nature research

https://doi.org/10.1038/s41565-020-00828-6

Supplementary information

Ultrafast hole spin qubit with gate-tunable spin–orbit switch functionality

In the format provided by the authors and unedited

Supplementary Information for Ultrafast Hole Spin Qubit with Gate-Tunable Spin-Orbit Switch Functionality

Florian N. M. Froning* , Leon C. Camenzind* , Orson A. H. van der Molen , Ang Li , Erik P. A. M. Bakkers , Dominik M. Zumbühl† , and Floris R. Braakman‡

This PDF file includes:

- Supplementary Notes 1 and 2
- Supplementary Figures 1 to 4
- Supplementary Table 1

*These authors contributed equally.
†Author to whom correspondence should be addressed. Electronic mail: dominik.zumbuhl@unibas.ch.
‡Author to whom correspondence should be addressed. Electronic mail: floris.braakman@unibas.ch.

1 Supplementary Note 1 Microwave Power Calibration

The transmission of the high-frequency part of the setup is frequency-dependent in the GHz regime. In addition to a continuously increasing attenuation at higher frequencies, there are also a number of pronounced, sharp, resonances where transmission is strongly attenuated due to impedance mismatch e.g. on the printed circuit board on which the sample is mounted. Changing the microwave frequency can therefore lead to a highly non-linear change of microwave power, thus affecting the Rabi frequency for these technical reasons (see Fig. 2**b** of the main text). Therefore, in order to acquire the data shown in Fig. 2**d** of the main text, we calibrate the microwave power arriving at the sample for each data point. To do so, we measure the linewidth of the zero-detuning line which is broadened due to inelastic tunneling assisted by the microwave drive on the gate [**Wiel2002**, **Nowack2007**]. In case of a dot-reservoir tunnel coupling Γ that is large in comparison to the drive frequency f_{MW}, applying a microwave tone predominantly leads to broadening and a power-dependent splitting with continuous shift of peak positions with applied microwave power. As shown in Figure S1, this results in a V-shaped dependence when detuning is plotted as a function of power. Here, $f_{\mathrm{MW}} = 3.75\,\mathrm{GHz}$, which corresponds to the datapoint at $|B_{\mathrm{ext}}| = 264\,\mathrm{mT}$ in Fig. 2**d** of the main text. We compare line cuts along the detuning axis to a reference measurement at $f_{\mathrm{MW}} = 6\,\mathrm{GHz}$ and $P_{\mathrm{MW}} = 25\,\mathrm{dBm}$ applied at the signal generator (blue dashed curve in Figure S1 **b**), and match the linewidth by adjusting P_{MW} for each f_{MW}. For the case of $f_{\mathrm{MW}} = 3.75\,\mathrm{GHz}$, shown in Figure S1, the reference linewidth is best matched for a power of 19 dBm (green curve). The highest (lowest) power which still gives a good overlap with the reference measurement (red curves in Figure S1 **b**) then determines the vertical error bars in Figure 2**d** in positive (negative) direction, where we assume a linear dependence of f_{Rabi} on A_{MW}.

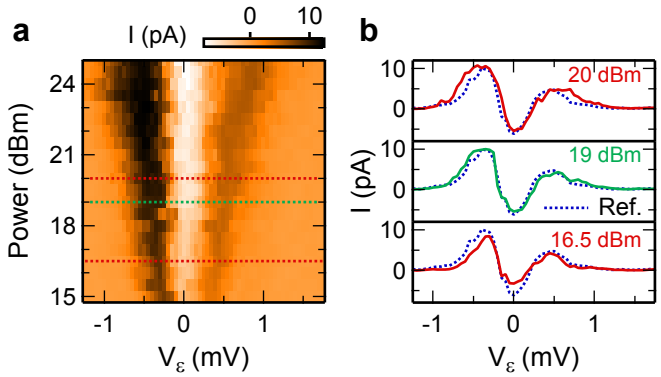

Figure S1: **Microwave power calibration.** **a** Linewidth measurement of the zero-detuning line with varying microwave power for calibrating the microwave power arriving at the sample. The drive frequency in this case is $f_{\mathrm{MW}} = 3.75\,\mathrm{GHz}$. **b** Line cuts along the detuning axis at different powers, as indicated in **a**. The reference measurement (blue dashed curve) corresponds to $f_{\mathrm{MW}} = 6\,\mathrm{GHz}$ and $P_{\mathrm{MW}} = 25\,\mathrm{dBm}$. Comparing the linewidth, the best match for $f_{\mathrm{MW}} = 3.75\,\mathrm{GHz}$ is found for $P_{\mathrm{MW}} = 19\,\mathrm{dBm}$ (green curve) and the upper (lower) limits are $P_{\mathrm{MW}} = 20\,\mathrm{dBm}$ (16.5 dBm), resulting in the error bars in Figure 2**d** of the main text.

2 Supplementary Note 2 Electrical Qubit Tunability

2.1 Tuning of Qubit Resonance with ΔV_P

For coherent manipulation with EDSR, the qubit is pulsed deeply into Coulomb blockade in order to protect it from unintended effects of the applied microwave burst. We measure EDSR for different pulse depths ΔV_P of the square voltage pulse which pulses the system into Coulomb blockade (see pulsing scheme depicted in Fig. 1 of the main text). Figure S2 shows the result as a function of the magnetic field $|B_\mathrm{ext}|$ and the pulse depth ΔV_P, while t_burst and f_MW are kept constant. The two vertical features in Figure S2 **a** at $\Delta V_\mathrm{P} = -0.1\,\mathrm{V}$ and $\Delta V_\mathrm{P} = 0.2\,\mathrm{V}$, between which the region of Pauli spin blockade is located (blue shaded area in Figure S2 **b** and **c**), correspond to the $T(1,1)$-$T(2,0)$ transition and the zero-detuning line of the bias triangle, respectively. The two curved features at $|B_\mathrm{ext}| = 320\,\mathrm{mT}$ and 360 mT correspond to the microwave induced $T_+(1,1) - S(1,1)$ and $T_-(1,1) - S(1,1)$ EDSR transitions, respectively.

For $-0.1\,\mathrm{V} \lesssim \Delta V_\mathrm{P} \lesssim 0.2\,\mathrm{V}$, spin manipulation takes place inside the bias triangle, leading to comparably bright features because charge transitions are not inhibited by Coulomb blockade, resulting in large interdot and dot-reservoir tunneling rates. The readout point, indicated by the green line in Figure S2 **b** and **c**, is positioned inside this area at $\Delta V_\mathrm{P} = 0\,\mathrm{V}$. For pulse amplitudes above $\Delta V_\mathrm{P} \gtrsim 0.2\,\mathrm{V}$, spin manipulation takes place inside Coulomb blockade, which prevents dot-reservoir tunneling during the microwave burst. This leads to the faint EDSR resonance indicated by the red dashed line in Figure S2 **a**. Note that due to the exchange interaction the resonance splits up for $\Delta V_\mathrm{P} \lesssim 0.35\,\mathrm{V}$.

Moreover, we observe a pronounced shift of the qubit resonance frequency as a function of the pulse depth ΔV_P, corresponding to a decrease of the g-factor. Figure S2 **b** shows a relative change of the g-factor by up to 20 % in a different gate configuration than the data shown in Figure S2 **a**. We emphasize here that when pulsing into Coulomb blockade, one must compensate for the induced change in g-factor at the manipulation point M. For a hole spin qubit tuned to be on resonance in the PSB region, the Coulomb pulse

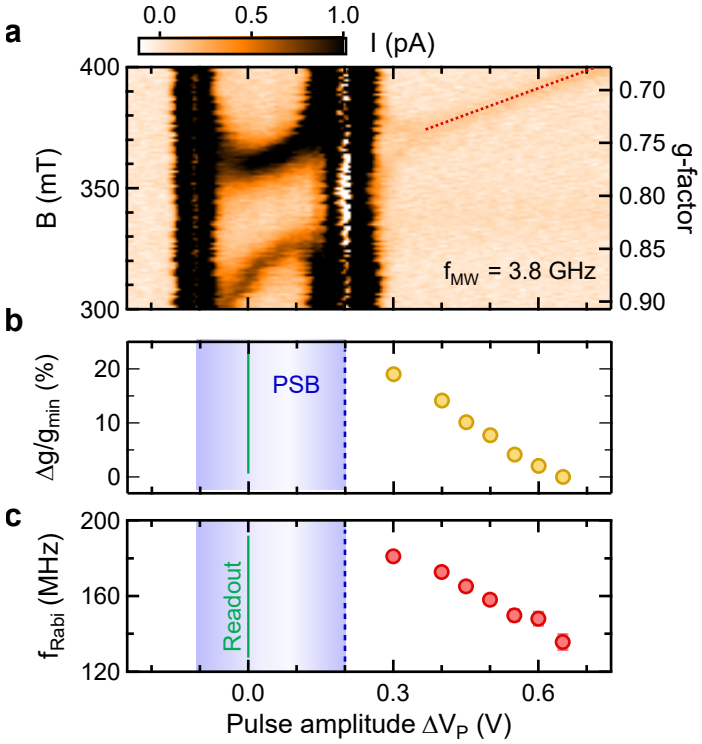

Figure S2: **Rabi frequency as a function of the Coulomb pulse amplitude.** **a** Measurement of the EDSR resonances as a function of magnetic field B_{ext} and Coulomb pulse amplitude ΔV_{P}. The microwave burst $t_{\mathrm{burst}} = 100\,\mathrm{ns}$, the frequency $f_{\mathrm{MW}} = 3.8\,\mathrm{GHz}$, and the power $P_{\mathrm{MW}} = 23\,\mathrm{dBm}$ are constant. When the spin manipulation is performed inside the Coulomb-blockaded region, the resonance signal is weak in intensity (red dashed line). **b, c** Relative change of g-factor and Rabi frequency as a function of the Coulomb pulse depth ΔV_{P} for a different dataset than shown in **a**. The region of Pauli spin blockade (shaded blue) and the readout point at $\Delta V_{\mathrm{P}} = 0\,\mathrm{V}$ (green line) are indicated.

will easily drive it far off-resonance, thus obliviating Rabi oscillations. Next, we measure the Rabi frequency for different values of ΔV_{P} along the red dotted line in Figure S2 **a** and find the results shown in Figure S2 **c**. The Rabi frequency is highest at manipulation points with small ΔV_{P} and decreases from 180 MHz to 130 MHz when increasing ΔV_{P}.

2.2 Electrical Tunability with V_{M}

The main text discusses the variation of the Rabi frequency due to changes of the voltage V_{M}. In addition to the spin-orbit length, also the electric field amplitude $|\vec{E}_{\mathrm{MW}}(t)|$, the g-factor and the orbital level splitting Δ_{orb} determine the Rabi frequency, which can be written as (see also equation (1) of the main text):

$$f_{\mathrm{Rabi}} = \frac{g_{\perp}}{g_{\parallel}} \cdot f_{\mathrm{MW}} \cdot \frac{l_{\mathrm{dot}}}{l_{\mathrm{so}}} \cdot \frac{e|\vec{E}_{\mathrm{MW}}(t)|l_{\mathrm{dot}}}{\Delta_{\mathrm{orb}}}. \tag{1}$$

Here, we used $f_{\mathrm{MW}} = |\vec{B}_{\mathrm{ext}}|g_{\parallel}\mu_B/h$, since we measure at constant microwave drive frequency f_{MW}, and $g_{\parallel}$ ($g_{\perp}$) to indicate the g-factor associated with the direction parallel (perpendicular, in the plane of $\vec{B}_{\mathrm{eff}}$ and $\vec{B}_{\mathrm{ext}}$) to the external magnetic field. We note that $l_{\mathrm{dot}} = \hbar/\sqrt{\Delta_{\mathrm{orb}} m_{\mathrm{eff}}}$ with the effective hole mass m_{eff}.

Because several quantities in equation (1) could depend on the gate voltages, we discuss the relative contributions of these individual terms to the 7-fold change of the Rabi frequency as observed in Figure 3**b** of the main text. We treat the contribution of the change in spin-orbit length l_{so} separately in section 2.2.1.

First, we investigate the contribution of the electric field amplitude, which can change as a function of V_{M} even at constant applied microwave power, due to changes of the quantum dot shape, size, or position, which may alter the electric dipole coupling. To roughly estimate the microwave electric field amplitude at the quantum dot for different configurations of V_{M}, we convert the voltage drop over gate V_{L} into an electric field across the quantum dot. The voltage drop, in turn, we determine from linewidth measurements of the modified zero-detuning line[**Nowack2007**], as discussed in section 1. We assume that the microwave voltage drops over 50 nm, corresponding to the distance between two neighboring gates. Figure S3 **a** shows the microwave electric field amplitude in the dot as a function of gate voltage V_{M} in the same range as used in the main text. Overall, the microwave electric field amplitude does not change significantly, which rules out an unintentional variation of the microwave power while changing the value of V_{M}.

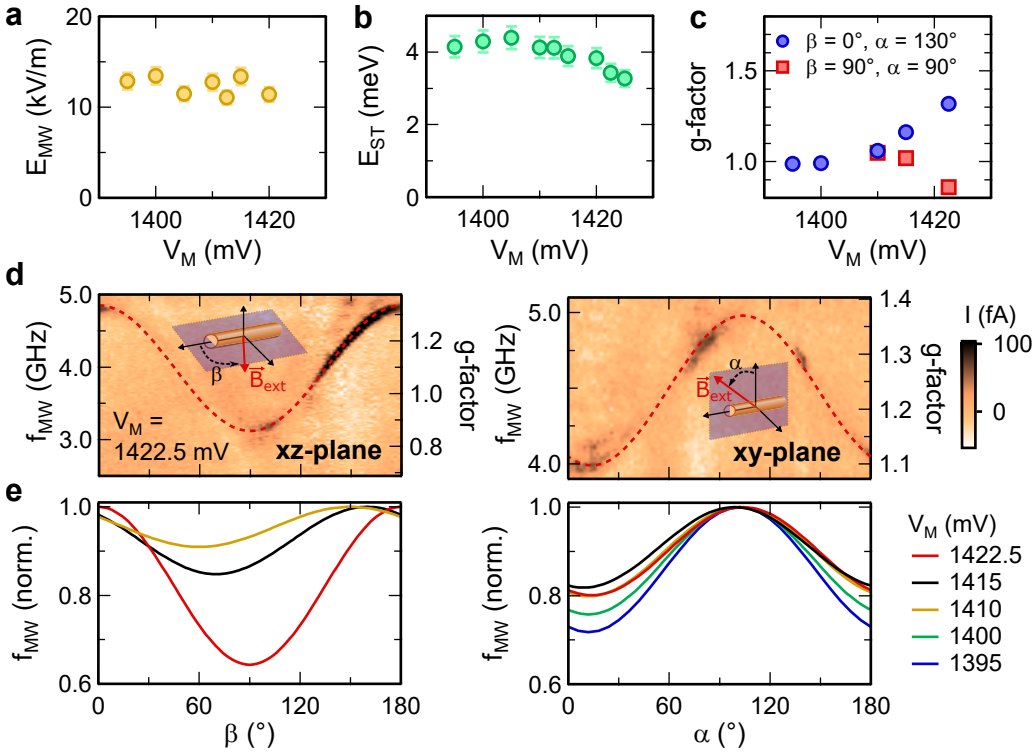

Figure S3: **Additional data supporting the qubit tunability with electric fields.** **a** Electric field strength of the microwave drive for different values of V_M in the same range as in Figure 3 of the main text. The values are extracted from the shift of the zero detuning line (see section 1) at the used microwave power $P = 11\,\mathrm{dBm}$. **b** Singlet-triplet splitting E_ST as a function of V_M extracted from line cuts in the bias triangle along the detuning line. **c** g-factor in perpendicular directions compared to the magnetic field orientation in Figure 3 of the main text. **d** Anisotropy measurements of the g-factor in the $\hat{x}\hat{z}$- (left) and $\hat{x}\hat{y}$- (right) plane for $V_\mathrm{M} = 1422.5\,\mathrm{mV}$ and $B_\mathrm{ext} = 260\,\mathrm{mT}$. The anisotropy is highlighted by the red dashed line. **e** From measurements as shown in **d**, the g-factor anisotropy in the $\hat{x}\hat{z}$- (left) and $\hat{x}\hat{y}$- (right) plane is extracted for several values of V_M. In order to compare differences of the g-factor anisotropy due to a change in V_M, each curve is normalized to its maximum.

Second, the Rabi frequency scales with the orbital level splitting Δ_orb roughly as $\sim 1/\Delta_\mathrm{orb}^2$ (see equation (1)). In order to estimate this contribution, we extract the single-dot singlet-triplet splitting E_ST for all values of V_M used in the main text and plot it in Figure S3 **b**. Note that $E_\mathrm{ST} = \Delta_\mathrm{orb} - E_\mathrm{exchange}$ includes contributions from both Δ_orb and the single-dot exchange energy E_exchange, which is not easily determined independently. In a realistic case, a more positive V_M increases both Δ_orb and E_exchange as the holes become more confined. Here, however, we disregard any changes in E_exchange as a function of V_M and

assign the observed decrease of E_{ST} in Figure S3 **b** solely to a change of Δ_{orb}. Note that this approach leads to an overestimation of the role of a change in Δ_{orb} with V_{M}. If the exchange energy indeed varies with V_{M}, the decrease of Δ_{orb} would be even smaller and therefore contribute less to the change in f_{Rabi}. If Δ_{orb} increases with V_{M}, it would even lead to a downward trend of f_{Rabi} with V_{M}.

We conclude that the reduction of the orbital level splitting Δ_{orb} from 4.1 meV to 3.3 meV can therefore maximally account for only a factor 1.5 out of the 7-fold increase of the Rabi frequency observed in the main text.

Lastly, the Rabi frequency also depends linearly on the g-factor $g_{\perp}$, as described by equation (1). This g-factor is perpendicular to $\vec{B}_{\mathrm{ext}}$ and lies in the plane defined by $\vec{B}_{\mathrm{eff}}$ and $\vec{B}_{\mathrm{ext}}$. It can also vary as a function of V_{M}, similar to the variation of $g_{\parallel}$ which is shown in Fig. 3**c** of the main text. However, extraction of $g_{\perp}$ is difficult in our case, because the orientation of $\vec{B}_{\mathrm{eff}}$ is unknown. In case of Rashba-type spin-orbit interaction, which can be expected to be dominant here, $\vec{B}_{\mathrm{eff}}$ points in a direction perpendicular to the electric field generating it and the hole momentum, which here is assumed to point along the nanowire, since the transverse confinement is very strong. The exact orientation of the electric field in our device, given by the voltages on the finger gates as well as the metallized contacts, is unknown, and therefore the direction of $\vec{B}_{\mathrm{eff}}$ cannot be stated with certainty.

However, from equation (1) we see $f_{\mathrm{Rabi}} \propto g_{\perp}/g_{\parallel}$. We can therefore conclude that an isotropic change of g-factors, would, for constant Zeeman energy, not lead to any change in the Rabi frequency. In the experiment of Fig. 3 of the main text, we indeed keep the Zeeman energy constant, because we measured at fixed drive frequency f_{MW} and therefore, in order to stay on resonance, compensate the variation of $g_{\parallel}$ (shown in Figure 3 **c** of the main text) with a proportional change of B_{ext} in the opposite direction.

In order to see the effect of the g-factor on the Rabi frequency, we therefore estimate the variation of the g-factor in two directions that are perpendicular to the orientation of $\vec{B}_{\mathrm{ext}}$ used to do the measurements in Figure 3 of the main text. Figure S3 **c** shows these g-

factors as function of V_{M}, extracted from measurements of the Larmor frequency. We find that the g-factor in the $\hat{x}\hat{z}$-plane (red dots in Figure S3 **c**) does not change significantly as a function of V_{M}. In the $\hat{x}\hat{y}$-plane (blue dots in Figure S3 **c**), we find that the g-factor increases as a function of V_{M} by a factor of 1.3.

This increase is somewhat less but comparable to the change of $g_{\parallel}$ in Figure 3**c** of the main text, which increases by a factor of 1.5 in the same range of V_{M}, indicating that the changes in g-factor are indeed rather isotropic.

These two directions, however, form only a subset of the entire plane perpendicular to $\vec{B}_{\mathrm{ext}}$. Although indicative of an isotropic change of g-factors, a full proof would entail determination of the complete g-matrix. Our measurements do not allow for such a full characterization, but we can give more indications for the g-matrix variation by providing measurements of the g-factor anisotropy in various planes, and as a function of V_{M}.

We measure the complete g-factor anisotropy in the $\hat{x}\hat{y}$ and in the $\hat{x}\hat{z}$ planes for a relevant range of V_{M}. Figure S3 **d** shows examples of such anisotropy measurements, for V_{M} =1422.5 mV. We extract the anisotropic g-factor, indicated by the red dashed curves, for different values of V_{M} as shown in Figure S3 **e**.

Each curve in Figure S3 **e** has been normalized to the maximum in order to better compare the change of the anisotropy. Overall, the g-factor anisotropy in the $\hat{x}\hat{y}$-plane decreases by about 10 % with increasing voltage V_{M}. Conversely, in the $\hat{x}\hat{z}$-plane the anisotropy increases by about 30 % with increasing voltage V_{M} and furthermore the position of the minimum g-factor shifts. While these changes in anisotropy are not negligible, they are small enough to indicate that variation of the g-factor in directions perpendicular to B_{ext} cannot solely account for the large variation of the Rabi frequency.

In conclusion, we estimate the contributions from changes in electric field amplitude (no change), orbital level splitting (factor of maximally 1.5), and the ratio $g_{\perp}/g_{\parallel}$ (factor of maximally 1.1) to account for a total of not more than a 1.7-fold change of the Rabi frequency. The very large change of the Rabi frequency by a factor of 7 can therefore be attributed mainly to an electrically tunable spin-orbit interaction, as expected from

a direct Rashba type of spin-orbit interaction. After estimating the impact of $|\vec{E}(t)|$, g-factor and Δ_{orb}, we now estimate the value of l_{so}.

2.2.1 Estimation of spin-orbit length

We estimate the spin-orbit length l_{so} using equation (1) directly from the measured Rabi frequency f_{Rabi}. Here, we use an effective value of l_{so} defined by $\pi l_{\mathrm{so}}/2$ being the length along the nanowire which a hole has to travel in order to have its spin flipped. This definition of l_{so} includes the possibility that the direction of the spin-orbit field $\vec{B}_{\mathrm{so}}$ with respect to the external magnetic field $\vec{B}_{\mathrm{ext}}$ can be non-optimal for EDSR, i.e. $\angle(\vec{B}_{\mathrm{so}}, \vec{B}_{\mathrm{ext}}) \neq 90°$. In this case, $|\vec{B}_{\mathrm{eff}}|$ assumes a smaller value, leading to lower Rabi frequencies than achievable with $\vec{B}_{\mathrm{so}} \perp \vec{B}_{\mathrm{ext}}$.

In our experiment, we do not determine the direction of $\vec{B}_{\mathrm{so}}$. However, values extracted for l_{so} from Eq. (1) of the main text using this effective definition correspond to upper bounds of the spin-orbit length defined in terms of the Rashba coefficient α as $\hbar/(m_{\mathrm{eff}}\alpha)$ as obtained by taking the optimal orientation $\vec{B}_{\mathrm{so}} \perp \vec{B}_{\mathrm{ext}}$. We estimate such upper bounds for l_{so} for four different values of V_{M}. The corresponding values of $|\vec{B}_{\mathrm{ext}}|$ are given by matching the Larmor frequency to f_{MW} and we determine the values of the remaining parameters $|E(t)|$, g, Δ_{orb}, and l_{dot} from other measurements. Note that these four values of V_{M} form a subset of those used in the main text.

The electric field amplitude $|E(t)|$ is estimated as described in section 2.2 and shown in Figure S3 **a**. Given the assumption that the entire voltage of the applied microwaves drops over the distance of 50 nm between neighbouring gates the value of $|E(t)| \approx 13\,\mathrm{kV\,m^{-1}}$ (see Figure S3 **a**) will result in conservative values for l_{so}, as taking a larger distance over which the voltage drops would result in a weaker electric field and hence larger l_{so}. For the g-factor and Δ_{orb} we take the values shown in Figures S3 **b** and **c**, which were obtained from anisotropy measurements and bias triangles, respectively. Note again that for determining Δ_{orb}, we neglect the exchange energy and a possible variation of it with V_{M}. Therefore, Δ_{orb} could be larger than we estimate here, which would make the

extracted values of l_{so} even smaller than those we find.

Lastly, to estimate the longitudinal dot length l_{dot}, we use $l_{dot} = \hbar/\sqrt{\Delta_{orb} m_{eff}}$, given an effective hole mass m_{eff}. For holes in Ge/Si nanowires, the effective mass depends strongly on the number of holes in the quantum dot[**Kloeffel2011**, **Kloeffel2018**]. Since we did not independently measure m_{eff}, we estimate l_{dot} and l_{so} both for m_{eff} being equal to the heavy-hole (HH) mass ($0.28\, m_0$, with m_0 the electron mass) and for m_{eff} being equal to the light-hole (LH) mass ($0.044\, m_0$). Table S1 and Fig. S4 present the calculated upper bounds for l_{dot} and l_{so} for the four different values of V_M. For the measurement with $V_M = 1422.5\,\text{mV}$, corresponding to the highest Rabi frequency, we find extemely short spin-orbit lengths of maximally 3 nm (20 nm) assuming a HH (LH) effective mass. Note that the fact that the current running through the double dot does not get significantly quenched even for high values of a magnetic field transverse to the nanowire (up to 6 T, not shown) points towards m_{eff} being rather closer to the HH mass than to the LH mass [**Froning2020**]. Further, note that for the relatively low microwave powers used here, equation (1) of the main text is valid even in the case that $l_{so} < l_{dot}$ [**BoscoPrivate2020**].

V_M (mV)	l_{dot} HH (nm)	l_{dot} LH (nm)	$\boldsymbol{l_{so}}$ **HH (nm)**	l_{so} LH (nm)
1395	8	21	**28**	177
1400	8	20	**19**	118
1410	8	21	**7**	47
1422.5	9	23	**3**	21

Table S1: Extracted values of l_{dot} and upper bounds of l_{so} for different values of V_M. Here LH (HH) corresponds to the case of a light-hole (heavy-hole) effective mass. The errors on all extracted values of l_{dot} and l_{so} are smaller than 15 %.

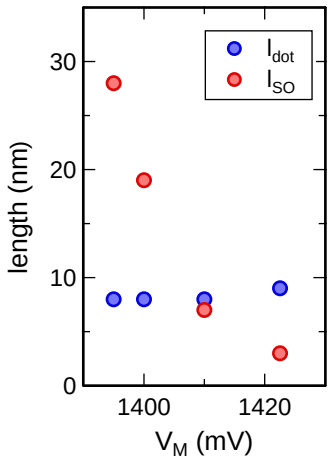

Figure S4: **Estimation of spin-orbit length and dot length.** Plot of l_{so} and l_{dot} as a function of V_{M}, estimated using measured values of g, Δ_{orb}, and $|E_{\mathrm{MW}}$ for each value of V_{M} as described in text. Here m_{eff} corresponds to the heavy-hole mass. Note that assuming another mass will change the absolute values of l_{so} and l_{dot}, but will leave the tunability with V_{M} unaffected.

References

[1] Conesa-Boj, S., Li, A., Koelling, S., Brauns, M., Ridderbos, J., Nguyen, T. T, Verheijen, M. A., Koenraad, P. M., Zwanenburg, F. A. & Bakkers, E. P. A. M. Boosting hole mobility in coherently strained [110]-Oriented ge-si core-shell nanowires, Nano Lett. **17**, 2259-2264 (2017).

[2] Van der Wiel, W. G., De Franceschi, S., Elzerman, J. M., Fujisawa, T., Tarucha, S., Kouwenhoven, L. Electron transport through double quantum dots, Rev. Mod. Phys. **75**, 1-22 (2002).

[3] Nowack, K. C., Koppens, F. H. L., Nazarov, Y. V. & Vandersypen, L. M. K. Coherent control of a single electron spin with electric fields, Science **318**, 1430-1433 (2007).

[4] Kloeffel, C., Trif, M. & Loss, D. Strong spin-orbit interaction and helical hole states in Ge/Si nanowires, Phys. Rev. B **84**, 195314 (2011).

[5] Kloeffel, C., Rančić, M. J. & Loss, D. Direct Rashba spin-orbit interaction in Si and Ge nanowires with different growth directions. Phys. Rev. B. **97**, 235422 (2018).

[6] Froning, F. N. M., Rančić, M. J., Hetényi, B., Bosco, S., Rehmann, M. K., Li, A., Bakkers, E. P. A. M., Zwanenburg, F. A., Loss, D., Zumbühl, D. M. & Braakman, F. R. In preparation (2020).

[7] Private communication with S. Bosco and D. Loss.